Ceramics International 50 (2024) 282–292

Contents lists available at ScienceDirect

Ceramics International

journal homepage: www.elsevier.com/locate/ceramint

Reaction path in the mechanosynthesis of calcium phosphates using a biogenic calcium source

Alberto C. Ferro [a,c], Tomás Seixas [a,c], Mafalda Guedes [b,c,*]

[a] Department of Mechanical Engineering, Instituto Superior Técnico, ULisboa, Av. Rovisco Pais, 1049-001, Lisboa, Portugal
[b] Department of Mechanical Engineering, Instituto Superior de Engenharia de Lisboa, Instituto Politécnico de Lisboa, R. Conselheiro Emídio Navarro 1, 1959-007, Lisboa, Portugal
[c] CeFEMA, Instituto Superior Técnico, Av. Rovisco Pais, 1049-001, Lisboa, Portugal

ARTICLE INFO

Handling Editor: Dr P. Vincenzini

Keywords:
High energy milling
Biogenic raw-materials
Calcium phosphates mechanosynthesis
Powder characterisation
Biomedical applications

ABSTRACT

Calcium phosphates were produced by mechanosynthesis, using eggshell, H_3PO_4 and 6–83 wt%-H_2O. Mixtures were milled at 600 rpm during 0.5–12 h. Resulting calcium phosphates occur within specific milling domains; H_2O concentration determines onset and stability of monophasic hydroxyapatite. Within the tested conditions, brushite is the first detected calcium phosphate precipitated from solution. In 6, 40 and 56 wt%-H_2O, monetite intermediates brushite's transformation to hydroxyapatite; in 71 and 83 wt%-H_2O transformation is direct. Hydroxyapatite formation is favoured at the H_2O extremes tested, 6 and 83 wt%. CO_2 build-up in the confined jar and nucleation-and-growth events during drying are possible obstacles upon control of morphology and composition of synthesised particles. The potential of chicken eggshell as direct biogenic source and the ability of high-energy milling as corresponding processing route to produce calcium phosphates was demonstrated. This signals a route for reliable production of brushite, monetite and hydroxyapatite. A preliminary milling map was built, allowing to obtain desired final product under specific milling conditions.

1. Introduction

Calcium phosphates (CaP) are salts of the triprotic acid H_3PO_4, i.e., they are calcium compounds (some of them hydrated) that contain $H_2PO_4^-$, HPO_4^{2-} or PO_4^{3-} ions [1]. CaP composed of $H_2PO_4^-$ only form under very acidic conditions, and therefore are not usually found in biological systems [1]; those based on HPO_4^{2-} and PO_4^{3-} correspond to the inorganic part of most human hard tissues [2]. There are twelve CaP in the CaO–P_2O_5–H_2O system (listed as supplementary material, Table S1), with variable Ca/P ratio, solubility and stability sensitivity to pH and temperature [3]. They are biocompatible and bioactive, promoting osteoconductivity, osteointegration and effective cell recruitment and proliferation. Also, thermodynamic stability in body fluids can be tailored through composition to render inert, bioactive and bioresorbable materials [4–8]. This makes synthetic CaP prevalent materials in bone tissue engineering (BTE) applications [4,5,9,10]. Current uses include bone substitution and filling, bone cements and remineralization intermediates, coating on orthopaedic implants and grafts for spinal fusion [6,8].

A range of dry, wet and high-temperature chemical processes render synthetic calcium phosphates by reaction between calcium and phosphate sources [7]. Among them, precipitation from reaction in the CaO–P_2O_5–H_2O system appears to be the most straightforward and cost-effective [11–16]. Yet, room temperature reaction kinetics is slow and calcium consumption is incomplete, hindering the development of monophasic domains. In the current work, $CaCO_3$ (calcite polymorph) is directly used as calcium source and aqueous solutions of H_3PO_4 provide both the phosphate group and H_2O. The synthesis reaction is triggered by dissociation of the triprotic orthophosphoric acid in aqueous solution, with solution pH value dictating the relative concentration of the protonated acid form and of the conjugated orthophosphate bases present (reaction 1) [15].

$$\mathbf{H_3PO_4} \overset{pKa_1=2.12}{\rightleftarrows} \mathbf{H_2PO_4^-} + \mathbf{H^+} \overset{pKa_2=7.21}{\rightleftarrows} \mathbf{HPO_4^{2-}} + \mathbf{2H^+} \overset{pKa_2=12.67}{\rightleftarrows} \mathbf{PO_4^{3-}} + \mathbf{3H^+} \quad (1)$$

Calcite solubility in aqueous solutions increases with the presence of H_3PO_4 [17] via reactions 2.1 to 2.3 [18,19].

* Corresponding author. Department of Mechanical Engineering, Instituto Superior de Engenharia de Lisboa, Instituto Politécnico de Lisboa, R. Conselheiro Emídio Navarro 1, 1959-007, Lisboa, Portugal.
E-mail address: mafalda.guedes@isel.pt (M. Guedes).

https://doi.org/10.1016/j.ceramint.2023.10.102
Received 15 June 2023; Received in revised form 9 October 2023; Accepted 11 October 2023
Available online 26 October 2023

$$CaCO_3 + H^+ \overset{pH<9.4}{\rightleftarrows} Ca^{2+} + HCO_3^- \quad (2.1)$$

$$HCO_3^- + H^+ \overset{6.5<pH<3}{\rightleftarrows} CO_2 + H_2O \quad (2.2)$$

$$HCO_3^- + H_2O \overset{pH>3}{\rightleftarrows} H_2CO_3 + OH^- \quad (2.3)$$

At constant temperature, calcium- and phosphate-containing solutions can be supersaturated with respect to different CaP phases depending on pH [15]. The molar fraction of each CaP formed is linked to the relative concentration of the dominant conjugated base resulting from H_3PO_4 stepwise dissociation (reaction 1) [15,20]. Thermodynamic equilibrium is thus expected to be reached through a sequence of reactions, that in the case of compositions with Ca/P = 1.67 M ratio culminates in hydroxyapatite (HA) formation [11,15,21,22]. Under very acidic initial conditions (pH < 2), the first CaP phase to precipitate is monocalcium phosphate monohydrate (MCPM, Ca/P = 0.5) (reaction 3) [13,20]. When pH reaches pH 2, formation of dicalcium phosphate dihydrate DCPD (brushite, Ca/P = 1.0) takes place through reaction 4 [11–13,15] and/or directly from solution (5) [23]. Meanwhile, continuous dissolution of calcite (reaction 2.1) continuously increases pH (up to pH > 4.2), allowing DCPD transformation into HA (reaction 6) [23].

$$Ca^{2+} + 2H_2PO_4^- + H_2O \overset{pH<2}{\rightleftarrows} \underset{MCPM}{Ca(H_2PO_4)_2 \cdot H_2O} \quad (3)$$

$$Ca^{2+} + \underset{MCPM}{Ca(H_2PO_4)_2 \cdot H_2O} + 3H_2O \overset{2<pH<4.2}{\rightleftarrows} 2\underset{DCPD}{(CaHPO_4 \cdot 2H_2O)} + 2H^+ \quad (4)$$

$$Ca^{2+} + H_2PO_4^- + OH^- + H_2O \overset{4.2\leq pH<6.5}{\rightleftarrows} \underset{DCPD}{CaHPO_4 \cdot 2H_2O} \quad (5)$$

$$\underset{DCPD}{10CaHPO_4 \cdot 2H_2O} + 4OH^- \overset{pH>4.2}{\rightleftarrows} \underset{HA}{Ca_{10}(PO_4)_6(OH)} + 4H_2PO_4^- + 22H_2O \quad (6)$$

However, due to determinant kinetic factors, precipitation of metastable CaP phases from solution is also possible [1,11,13,15,21,22]. DCPD's extremely slow reaction requires extended solution/solid balance for equilibrium to be reached via reaction 6, which prevents direct conversion to HA [11,15]. Instead, HA formation tendentially takes place through precipitation of more acidic intermediate phases [12,15,24,25], namely DCPA (monetite, Ca/P = 1.0) (reactions 7 [26] and 8 [13]) [11,15] and/or octacalcium phosphate (OCP, Ca/P = 1.33) (reactions 9 [27] and 10 [15]) [13,28].

$$\underset{DCPD}{CaHPO_4 \cdot 2H_2O} \overset{pH>4.2}{\rightleftarrows} \underset{DCPA}{CaHPO_4} + 2H_2O \quad (7)$$

$$\underset{DCPA}{10CaHPO_4} \overset{pH>4.2}{\rightleftarrows} \underset{HA}{Ca_{10}(PO_4)_6(OH)_2} + P_4O_{10} + 4H_2O \quad (8)$$

$$\underset{DCPD}{8CaHPO_4 \cdot 2H_2O} \overset{6.5<pH<8}{\rightleftarrows} \underset{OCP}{Ca_8(HPO_4)_2(PO_4)_4 \cdot 5H_2O} + 2H_3PO_4 + 11H_2O \quad (9)$$

$$\underset{OCP}{Ca_8(HPO_4)_2(PO_4)_4 \cdot 5H_2O} + 2Ca^{2+} \overset{8.0<pH<10.0}{\rightleftarrows} \underset{HA}{Ca_{10}(PO_4)_6(OH)_2} + 3H_2O + 4H^+ \quad (10)$$

Reactions 7 and 8 are enabled when the balance between H^+ release rate in reactions 1 and 4 and the proton consumption rate in ongoing reaction 2.1 renders a pH net increase [15]. DCPD conversion towards HA (reaction 6) can take place when pH > 6.5 [15]. Similarly, OCP reactions 9 and 10 are enabled above pH 8 [15]. Above pH ~ 10 direct HA precipitation is enable (reaction 11) (Ca/P = 1.67) [3,15].

$$10Ca^{2+} + 6PO_4^{3-} + 2OH^- \overset{8.0<pH<10.0}{\rightleftarrows} \underset{HA}{Ca_{10}(PO_4)_6(OH)_2} \quad (11)$$

Nevertheless, direct HA precipitation from solution is very slow, and reaction 11 is tendentially incomplete [1,13,15]. The necessary energy to overcome the kinetic barrier is most frequently supplied in the form of temperature and pressure (hydrothermal synthesis) [7,29,30]. Yet, the existence of kinetic issues clearly evokes another approach - mechanosynthesis. Similarly to conventional wet synthesis, wet CaP mechanosynthesis takes place through the described sequence of dissolution-reprecipitation reactions [31]. However, in high-energy milling mechanosynthesis chemical reactions are promoted at room temperature. They are fostered by fast intimate mixing between reactants, and creation of fresh surfaces, defects and active sites, enabling significant reactivity increase [32,33]. Also, the inherent reduction of precipitate particle size allows the production CaP particles with submicron/nanometric size, which have been reported to exhibit enhanced resorbability, bioactivity and release of calcium ions when compared to micrometric CaP available from conventional synthesis [34–37].

Regardless of the production route, synthetic CaP are mostly stoichiometric [7]. Yet, bone hydroxyapatite is poorly crystalline, calcium-deficient, and includes a number of trace metal ion substitutions that promote osteoblast formation and bone adhesion (e.g., Mg^{2+}, Sr^{2+}) [38,39] and increase material solubility and resorbability [40]. The current work approaches this issue by using calcium carbonate of biogenic origin (chicken eggshell) as the calcium source. On average, the shell of the eggs of domestic chicken (*Gallus domesticus*) contains approx. 96 wt % calcite, 1 wt% $MgCO_3$, and trace N^+, Na^+, Mg^{2+} and Sr^{2+} [39,41]. The combined use of mechanosynthesis and eggshell as a viable route for direct production of synthetic HA and β-tricalcium phosphate (β-TCP) with crystalline structure and composition similar to that of human hard tissues was first described in 2003 [42]. Since then, few studies were reported (supplementary material, Table S2), and only recently the need for previous calcite calcination and/or thermal treatment of the milled powder was dismissed [43,44].

In the described context, this report is part of an ongoing systematic effort to study the influence of operational milling parameters upon the CaP compositions formed in the $CaCO_3$–H_3PO_4–H_2O system. In this work, only limited consideration is given to post-milling effects and the focus is set on the build-up of information regarding the influence of milling parameters and water concentration on the composition of produced powders. Results along the composition line with Ca/P = 1.67 M ratio are reported and a preliminary milling map, adjusting experimental parameters to desired final product under specific conditions, is proposed.

2. Experimental

2.1. Materials

In all experiments, the calcium source ($CaCO_3$ calcite polymorph) was chicken brown eggshell gathered in domestic households. Eggshell was thoroughly washed under tap water, stripped from the inner protein membrane, and boiled in distilled water for 5 min. After drying, the shell was manually crushed in an agate mortar and characterised regarding particle size distribution (Cilas, 1064 L). The phosphate source was H_3PO_4 aqueous solution (85 wt%, Panreac).

Mixtures were formulated (Table 1) using deionised water and amounts of eggshell and phosphorus source complying with the Ca/P = 1.67 M ratio of stoichiometric hydroxyapatite. Materials handling prior to sealing of the milling vial was carried out under NPT conditions for all batches.

Table 1
Tested $CaCO_3$–H_3PO_4–H_2O compositions and milling times (600 rpm).

Sample designation	Tested milling time (h)	Composition (wt%)			Ca/P ratio (mol/mol)
		H_2O*	calcite	H_3PO_4	
W6-t_	0.5, 1, 2, 4, 6, 9, 12	6	59	35	1.67
W40-t_	0.5, 1, 2, 4, 6, 9, 12	40	38	22	
W56-t_	0.5, 1, 2, 4, 6, 9, 12	56	28	17	
W71-t_	0.5, 1, 2, 4, 6, 9, 12	71	19	11	
W83-t_	0.5, 1, 2, 4, 6, 9, 12	83	11	6	

*W_*: H_2O concentration in the initial system (wt%); t_: milling time (h).
*Water in the reagents' mixture, including water introduced via the commercial acid solution, but not including H2O resulting from H3PO4 decomposition.

2.2. Experimental procedure

The pH of each batch was measured (ADWA, AD1020) immediately after reagents mixing. High-energy mechanical milling took place in a planetary ball mill (Retsch, PM100). Alumina vial (250 ml) and balls (18 balls, ∅ 10 mm) were used, both from Retsch (maximum impurity <0.24 wt% according to supplier). The mass of the mixtures in each batch complied with 10:1 ball-to-powder mass ratio (BPR). Milling was always carried out at 600 rpm, for time periods ranging from 0.5 h to 12 h (Table 1). After milling, all suspensions were oven dried at 60 °C for 24 h. Microstructural studies were carried out using field emission gun scanning electron microscopy (FEG-SEM) (JEOL, JSM-7001 F) coupled to energy dispersive X-ray spectroscopy microanalysis (EDS) (Oxford Instruments, Inca pentaFETx3). Particle size of milled powders was evaluated via image analysis of at least five SEM micrographs at 1000× magnification, using *Image J* [45]. Micro-Raman confocal spectroscopy (Horiba Jobin-Yvon, HR Evolution) was used to identify CaP phases formed by mechanosynthesis and other phases otherwise present after milling. Spectra were collected in the 200-4000 cm^{-1} wavenumber range (for clarity's sake, spectra are only displayed up to 1200 cm^{-1}) with 5 accumulations and acquisition time of 10 s, using a 532 nm laser, 100× objective lens, 200 hole and 600 grooves/mm grating. The software FITYK 0.9.8 [46] was used for background removal, and peak fitting was carried out with Lorentzian function. Crystalline phases present in the powders were assessed by X-ray diffraction (XRD) using CuK_α radiation (D8 advance, Bruker), in the 5° to 65° 2θ range, with 0.02° step size and 4 s step time. (diffractograms are only displayed in the 5° to 40° 2θ region, that encompasses the first two most intense peaks of calcium phosphate phases). A knife set accessory was used to reduce the background level in the lower 2θ range. Raman spectroscopy and XRD were also used to characterise the starting materials. Raman and XRD data used for phase identification are provided as supplementary material (Tables S3.1 and S3.2).

3. Results

3.1. Characterisation of precursor materials

After manual crushing eggshell particles display size distribution in the micrometric range, with $d_{50} = 71.4 \pm 0.8$ μm. EDS elemental analysis confirmed the presence of Ca, C and O, as well as trace Mg (0.40 ± 0.02 wt%). Within the XRD experimental conditions used, the only crystalline phase identified in eggshell (Fig. 1a) was the $CaCO_3$ calcite polymorph (Fig. 1b). Raman results complemented this information: the displayed bands, around at 275, 713 and 1084 cm^{-1}, are consistent with the spectrum of calcite [47,48] (Fig. 1c, peaks labelled in bold). Comparison of eggshell spectrum with that of the protein membrane (Fig. 1d)

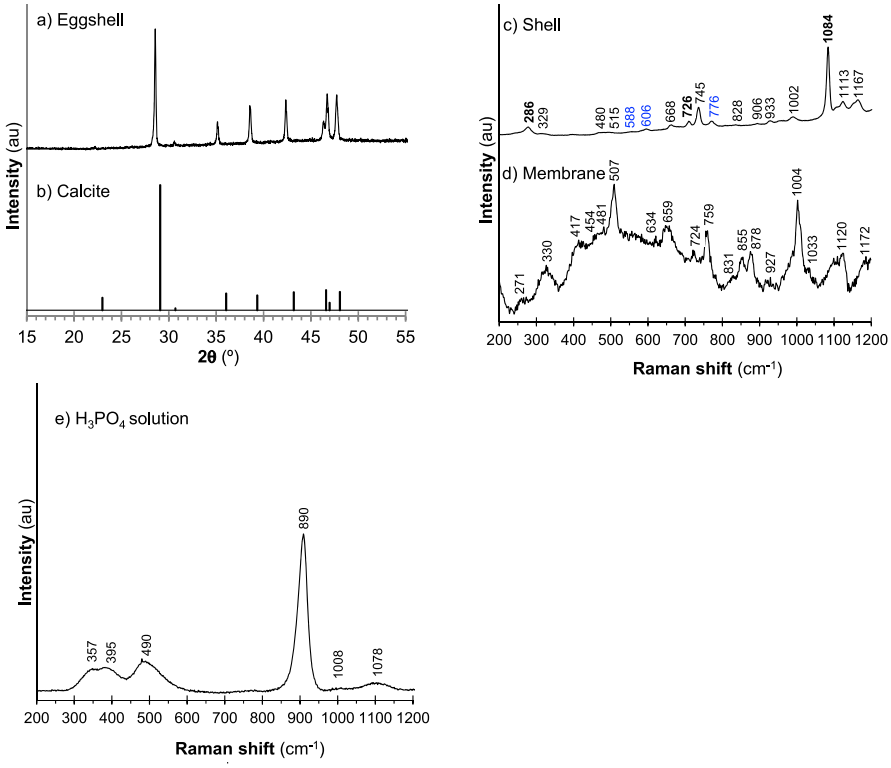

Fig. 1. Characterisation of reagents. XRD diffractograms of (a) as-cleaned chicken eggshell powder compared to (b) the ICDD pattern of pure calcite (file 01-86-2342). Raman spectra of (c) as-cleaned eggshell powder (bold: peaks corresponding to calcite; blue: protoporphyrin IX), (d) organic membrane removed from eggshell, and (e) 85 % H_3PO_4 aqueous commercial solution. (For interpretation of the references to colour in this figure legend, the reader is referred to the Web version of this article.)

indicates that, with few exceptions, the remaining bands can be assigned to remnants of the organic film. The very weak bands around 588, 606 and 776 cm^{-1} (Fig. 1c, in blue) were assigned to protoporphyrin IX, the main pigment in chicken brown eggshell [49]. The Raman spectrum of the H_3PO_4 commercial solution (Fig. 1e) is consistent with the bands of orthophosphoric acid in aqueous solution [50]. Within the XRD experimental conditions used, the only crystalline phase identified in eggshell (Fig. 1a) was the $CaCO_3$ calcite polymorph (Fig. 1b). Raman results complemented this information: observed bands with maxima at 275, 713 and 1084 cm^{-1} are consistent with the spectrum of calcite [47,48] (Fig. 1b, peaks label in bold). Comparison of eggshell spectrum with that of the protein membrane (Fig. 1d) indicates that, with few exceptions, the remaining bands can be assigned to remnants of the organic film. The very weak bands around 588, 606 and 776 cm^{-1} (Fig. 1c, in blue) were assigned to protoporphyrin IX, the main pigment in chicken brown eggshell [49]. The Raman spectrum of the H_3PO_4 commercial solution (Fig. 1e) is consistent with the bands of orthophosphoric acid in aqueous solution [50].

Since powder contamination from the milling media is an inherent drawback of mechanical milling [33], XRD and Raman data of alumina from the milling media (jar and balls) were also collected. Both the diffraction peaks (Fig. 2a) and the seven Raman bands displayed (Fig. 2c) match those of α-Al_2O_3 [51] (Fig. 2b, ICCD 46–1212 data file).

3.2. Phase composition of milled powders

Results regarding the effect of milling time and H_2O concentration upon phase composition and crystalline phases present in milled dry powders were obtained by Raman spectroscopy and powder XRD (Figs. 3–7). Each figure groups data obtained for the same water concentration value (W) and all tested milling times. It should be mentioned that detection of solvated H_3PO_4 [50] (supplementary Table S3.3) is associated to high uncertainty, since its most intense Raman bands (850 and 898 cm^{-1}) overlap those of DCPD and DCPA. Also, the most intense diffraction peaks overlap those of calcite, DCPD and HA (31.1° and 29.7°) or are seldom present (24.1°).

Raman spectra of W6 powders (Fig. 3a) show that milling bellow at least 1 h yields a mixture of unreacted calcite and H_3PO_4 [47,48], DCPD (fingerprint bands around 986 and 878 cm^{-1} [52,53]) and DCPA (988 and 902 cm^{-1} [52,53]). Between 1 h and 2 h, HA (960 cm^{-1} [53]) onset takes place. Calcite, H_3PO_4, DCPD, DCPA and HA coexist up to at least 6 h. Reactions involving calcite, H_3PO_4 and DCPD are complete for 9 h milling. DCPA exhausts between 9 h and 12 h, rendering a monophasic HA domain. These results are confirmed by XRD data (Fig. 3b).

W40 powders milled bellow at least 4 h render a mixture of calcite, H_3PO_4 and DCPD. Phase's composition evolution requires longer times than W6 (between 4 h and 6 h) for DCPA and HA formation onset, while the intensity of DCPA and of HA Raman bands (Fig. 4a) and diffraction peaks (Fig. 4b) suggest that their concentration is very low at all times.

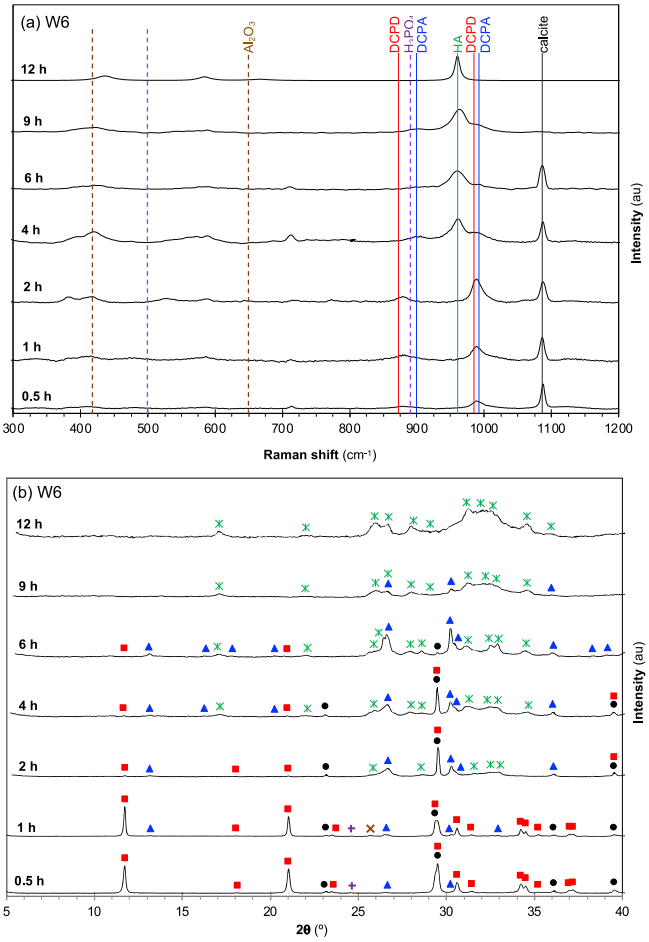

Fig. 3. Effect of increasing milling time on W6 composition. a) Raman spectra (the most intense band for each phase is signalled with the phase's name; unlabelled bands are common to several CaP [30] and could not be unravelled). b) X-ray diffractograms (● calcite, ■ DCPD, ▲ DCPA, ★ HA, x Al_2O_3, + H_3PO_4).

Calcite, H_3PO_4, DCPD and DCPA consumption is incomplete up to 12 h milling (inclusive). This also corresponds to the evolution of phase composition in W56 (Fig. 5a and b).

In W71 powders (Fig. 6a and b) HA was detected as soon as 1 h, together with calcite, H_3PO_4 and DCPD, coexisting up to at least 9 h. For longer milling (12 h), calcite, H_3PO_4 and HA coincide and DCPD is no longer identified. In W83 milled powders, the phases present up to 6 h (inclusive) comprise H_3PO_4, calcite, DCPD and HA. Above at least 6 h milling, reaction involving H_3PO_4, calcite and DCPD are complete, and a monophasic HA domain is identified.

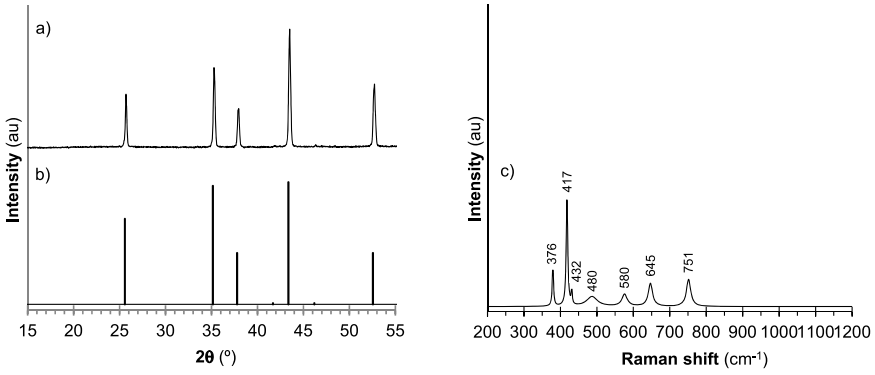

Fig. 2. Characterisation of milling media materials: (a) XRD diffractogram, compared to (b) the ICCD file of pure α-alumina (46–1212). (c) Raman spectrum.

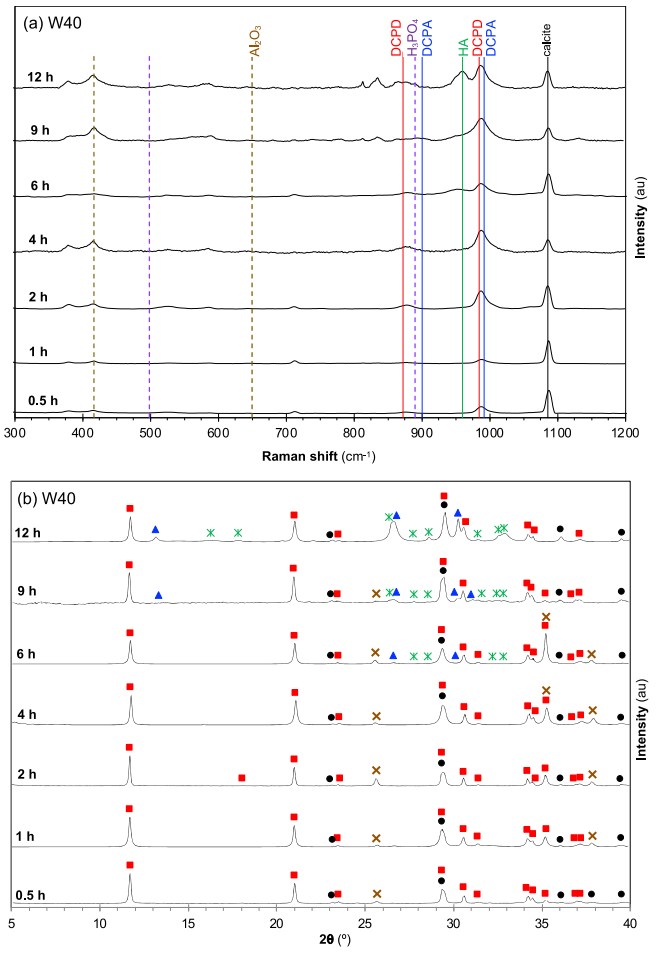

Fig. 4. Effect of increasing milling time on W40 composition. a) Raman spectra (the most intense band for each phase is signalled with the phase's name; unlabelled bands are common to several CaP [30] and could not be unravelled). b) X-ray diffractograms (● calcite, ■ DCPD, ▲ DCPA, ✱ HA, x Al_2O_3, + H_3PO_4).

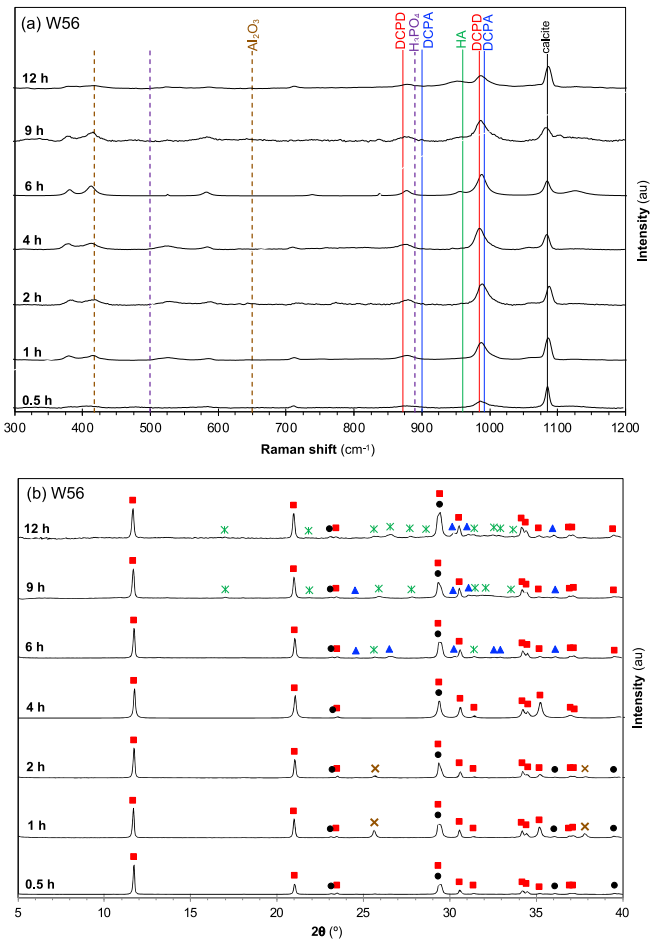

Fig. 5. Effect of increasing milling time on W56 composition. a) Raman spectra (the most intense band for each phase is signalled with the phase's name; unlabelled bands are common to several CaP [30] and could not be unravelled). b) X-ray diffractograms (● calcite, ■ DCPD, ▲ DCPA, ✱ HA, x Al_2O_3, + H_3PO_4).

XRD results (Figs. 3b–7b) are in general agreement with the corresponding information delivered by Raman spectroscopy (Figs. 3a–7a). Most diffractograms present sharp and well-defined diffraction peaks and low noise, typical of highly crystalline materials (e.g., Fig. 4c up to W56-t6). In some systems, due to particle comminution to the nanosize, XRD peaks broaden as milling time increases (e.g., W71-t9 and W71-t12), tending to display broad diffraction humps [54,55]. The absence of the Raman band characteristic of amorphous calcium phosphates, around 950 cm^{-1} [54], excluded its assignment to the presence of amorphous calcium phosphates [54].

Overall, results in Figs. 3–7 indicate that DCPD, DCPA and HA were the only calcium phosphate phases detected within the tested milling conditions. HA is often present in incipient amount, while monophasic HA domains were achieved at the extreme H_2O concentration and the maximum milling times tested (samples W6-t12, W6-t9 and W83-t12). It should be mentioned that alumina Raman modes and diffraction peaks were identified in most powders, indicating contamination from the milling media.

3.3. Size and morphology of produced powders

SEM observation of milled powders after oven drying suggests a profound effect of milling time and batch water concentration on the developed particle morphology. The observed particle shapes can be broadly grouped as irregular spheres (Fig. 8a and b) or plates (Fig. 8c–e), with sizes ranging from a few nanometers (mainly spheres, e.g.: Fig. 8a) to some microns (mostly plates, e.g., Fig. 8c).

Synthesised monophasic HA (samples W6-t12, W83-t9 and W83-t12) forms irregular spheres in the nanometric size range, whereas DCPA appears as irregular nanospheres and DCPD particles display shape and dimensionality variety. This includes nanospheres (Fig. 8a) and submicrometric spheres (Fig. 8b), irregular nanometric (Fig. 8c) and micrometric plates (Fig. 8d) and micrometric tabular plates (Fig. 8e), and more complex flower-like agglomerates built from individual nanoplatelets (Fig. 8f).

The influence of milling time on d_{50} values for all systems is depicted in Fig. 10. As expected, a predominant trend towards smaller d_{50} values is observed with milling time increase. However, in all systems, an increase from 0.5 h to 1 h milling takes place, particularly in system W83. Also, system W40 displays an abnormal behaviour showing an almost constant small increase of d_{50} value with milling time.

During milling, crystallization and fragmentation take place simultaneously and, crystal growth is thus hampered by the imposed fragmentation [16,56–59]. As milling proceeds, the resulting particles are expected to display reducing nano-submicrometric size and narrower size distribution [58,59]. However, besides the already mentioned abnormal behaviour, most batches include a variety of particle size standard deviations (Fig. 9) and shapes (e.g., Fig. 8d). These results suggest that secondary drying products were obtained in addition to primary milling products: the large and complex morphologies displayed (e.g., Fig. 8f) are expected to result from undisturbed growth, necessarily taking place during post-milling drying. This effect clearly

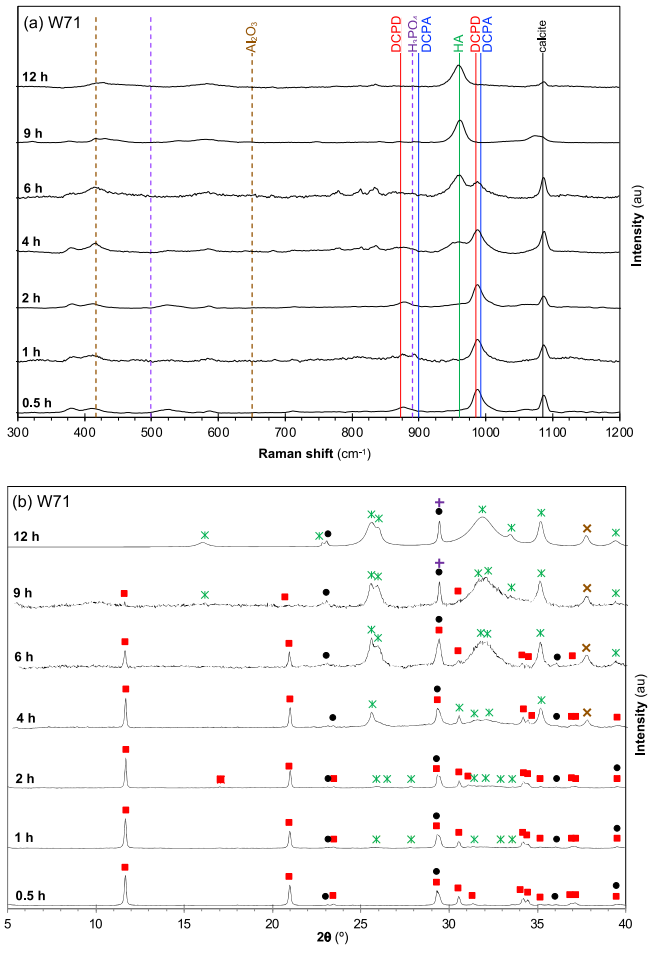

Fig. 6. Effect of increasing milling time on W71 composition. a) Raman spectra (the most intense band for each phase is signalled with the phase's name; unlabelled bands are common to several CaP [30] and could not be unravelled). b) X-ray diffractograms (● calcite, ■ DCPD, ▲ DCPA, ★ HA, x Al_2O_3, + H_3PO_4).

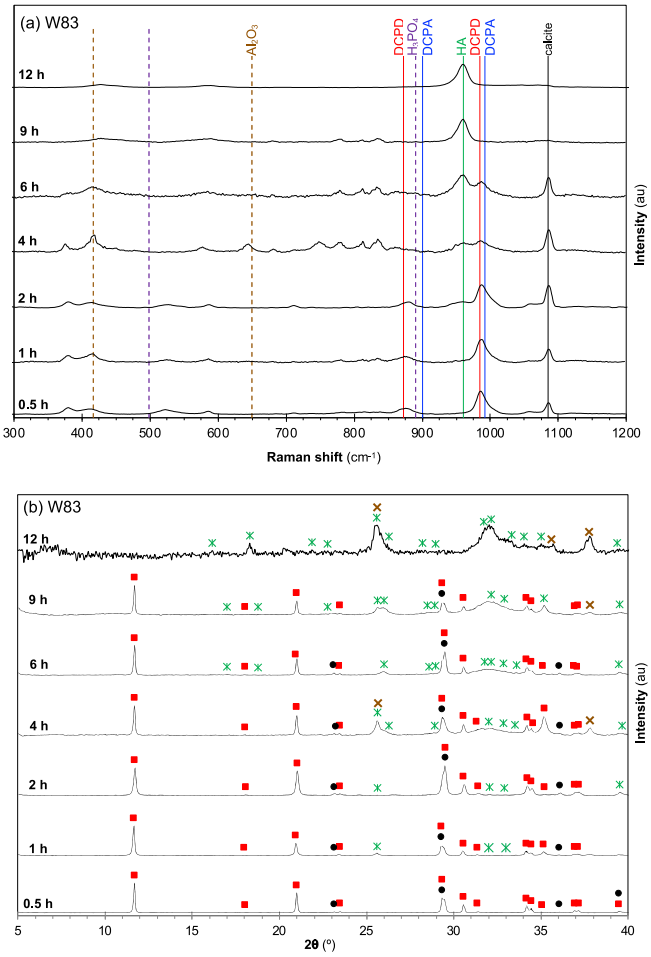

Fig. 7. Effect of increasing milling time on W83 composition. a) Raman spectra (the most intense band for each phase is signalled with the phase's name; unlabelled bands are common to several CaP [30] and could not be unravelled). b) X-ray diffractograms (● calcite, ■ DCPD, ▲ DCPA, ★ HA, x Al_2O_3, + H_3PO_4).

indicates that the development of tailored compositions with dedicated morphology and narrow particle size range requires strict control of drying parameters, including drying temperature and cooling rate [29]. Further work is ongoing to differentiate the effect of milling parameters from those of drying conditions upon formed CaP phase composition and morphology.

Albeit the effect that secondary drying may have upon the measured size and morphology of the produced CaP it is possible to conclude that, above 4 h milling, particles obtained in the current work vary predominantly from the nanometric range (systems W6, W56 and W71) to the submicrometric and micrometric range (respectively, W83 and W40) and, thus, approximately two orders of magnitude smaller than those resulting from conventional wet chemical synthesis. Also, synthesised monophasic HA (W6-t12 and W83-t12) and DCPA (e.g., W6-t6) particles appear as irregular nanospheres, while DCPD particles display shape and dimensionality variety. DCPD particles have been reported to exhibit tabular to needle-like crystals in the 10–130 μm range, with flower-like structures in the 10–100 μm range [60,61]. The current work rendered DCPD plates in the 50–300 nm range and flower-like structures with 3–5 μm diameter. Reported DCPA crystals typically display micrometric rod like morphology and large variations in size [62,63], whereas the produced DCPA particles are nanospheres in the 100–200 nm range (Fig. 6b). Also, produced HA nanospheres display a noticeable consistent nanosize diameter in the 20–200 nm interval, much narrower than those precipitated by conventional wet synthesis, with reported values between 5 nm and several hundred micron [7]. Supplementary material S4 details obtained particle's shape and dimensionality.

4. Mechanochemical paths in studied $CaCO_3$–H_3PO_4–H_2O compositions

The hypothesis put forward in the current work is that mechanical milling can provide the energy required to unleash room temperature formation of the thermodynamically stable phases in the $CaCO_3$–H_3PO_4–H_2O system. For this purpose, biogenic calcite (chicken eggshell) and orthophosphoric acid solution complying with Ca/P = 1.67 M ratio were used and ball milled during 0.5 h–12 h, at 600 rpm, in the presence of variable amounts of water (6–83 wt%). Obtained results demonstrate the overall potential of calcite in chicken eggshell as a natural calcium source for the mechanochemical production of calcium phosphates, as well as the adequacy of high-energy milling to produce calcium phosphate phases at room temperature, including HA.

The milling map in Fig. 10 summarises the phases identified in the dried milled powders versus milling time and water concentration. It stresses that, besides the milling energy deliver to the powders, water content plays a major role both on the sequence of CaP formed an on the onset of HA formation and its stability limits. DCPA is only present in W6 (t2 to t9 samples), and W40 and W56 (t6 to t12 samples) systems; DCPD is present in all systems. HA onset varies with the water concentration value and milling time (0.5 h for W83; 1 h for W71; 2 h for W6; 6 h for W40 and W56). Apparently monophasic HA domains, corresponding to

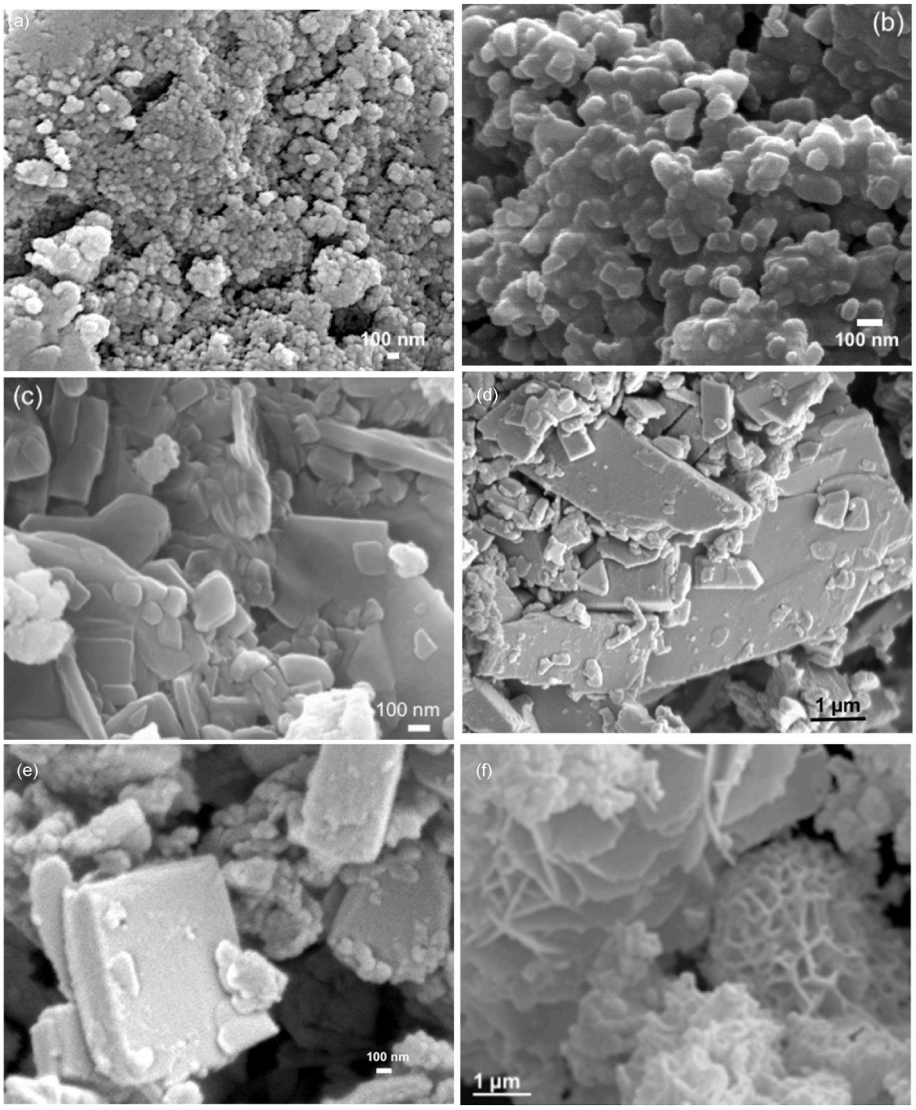

Fig. 8. Examples of particle morphology in obtained powders. Irregular spheres: (a) nanometric (W6-t6) and (b) submicrometric (W6-t05). Plates: (c) irregular nanometric and submicrometric (W6-t1) and (d) irregular micrometric plates (W83-t1) (low magnification image). Other, rarer, morphologies: (e) tabular plates (only detected in W56-t9); (f) flower-like agglomerated platelets (only identified in W56-t4) (low magnification image).

fully reacted samples, without the presence of $CaCO_3$ and H_3PO_4, were only identified for the extreme water concentration systems (W6 and W83) for the higher milling time tested.

The measured pH value of the batches after initial mixture of reagents (before milling), ranged from 0.26 (W6) to 0.96 (W71 and W83). Yet, while reaction 3 (MCPM formation) is expected to occur below pH 2 [13,20], MCPM was never detected. This is in good agreement with results on a similar system, $15CaCO_3$–$9H_3PO_4$–$76H_2O$ (in between W71 to W83 compositions in the current work), submitted to mechanical stirring at 400 rpm [13]: the low initial pH (0.8) rapidly increased, due to MCPM formation (reaction 3), to reach pH 2 (9 min) (necessary for the onset of DCPD formation) and its full conversion of MCPM (reaction 4) (19 min) [13]. In the current study, the energy provided to the system is much higher, and thus expected to accelerate the sequence of dissolution-reprecipitation reactions, hindering the detection of MCPM [13,16,64,65]. The onset of DCPD transformation into other CaP (enabled above pH 4.2 [13,66]), takes place when the rate of reaction 2.1 (H^+ consumption from solution) surpasses the rate of reaction 4 (H^+ release to solution) [13].

In the W6 system, the low water concentration is expected to prevent extended dissociation of H_3PO_4, resulting in pH increase. As a result, despite released protons toil in calcite dissolution via reaction 2.1, this reaction's progress is limited. Water concentration is also below the stoichiometric requirement for full Ca^{2+} consumption via reactions 3 and 4, thus the formation of MCPM followed by DCPD is restrained. Together, this results in small $CaCO_3$ consumption, together with a narrow (below 2 h) corresponding DCPD stability domain, which renders conditions for the onset of DCPA precipitation (reaction 7) [21]. In this system DCPD and DCPA formation was identified at 0.5 h. Both Raman (Fig. 3a) and XRD (Fig. 3b) results show only a small change in peak intensity, suggesting that the rate of DCPD formation (reaction 5) is low. Between 1 h and 2 h, reactions 7 and 8 are triggered [13] and for 2 h milling time, DCPA is the main CaP present, accompanied by DCPD (almost exhausted) and HA (trace). Between 2 h and 4 h, reaction 8 starts to dominate over reaction 7, and HA fraction increases significantly. At 9 h DCPA is the only other phase present and at 12 h a stable apparently monophasic HA domain is attained.

In all other systems H_2O concentration surpass the stoichiometric requirement for reactions 3 and 4 completion. Yet, W40 and W56 still require DCPA to intermediate HA formation, with apparently similar reaction sequence and time frame. The increase of H_2O concentration in these systems leads to progressive decrease of the DCPA stability

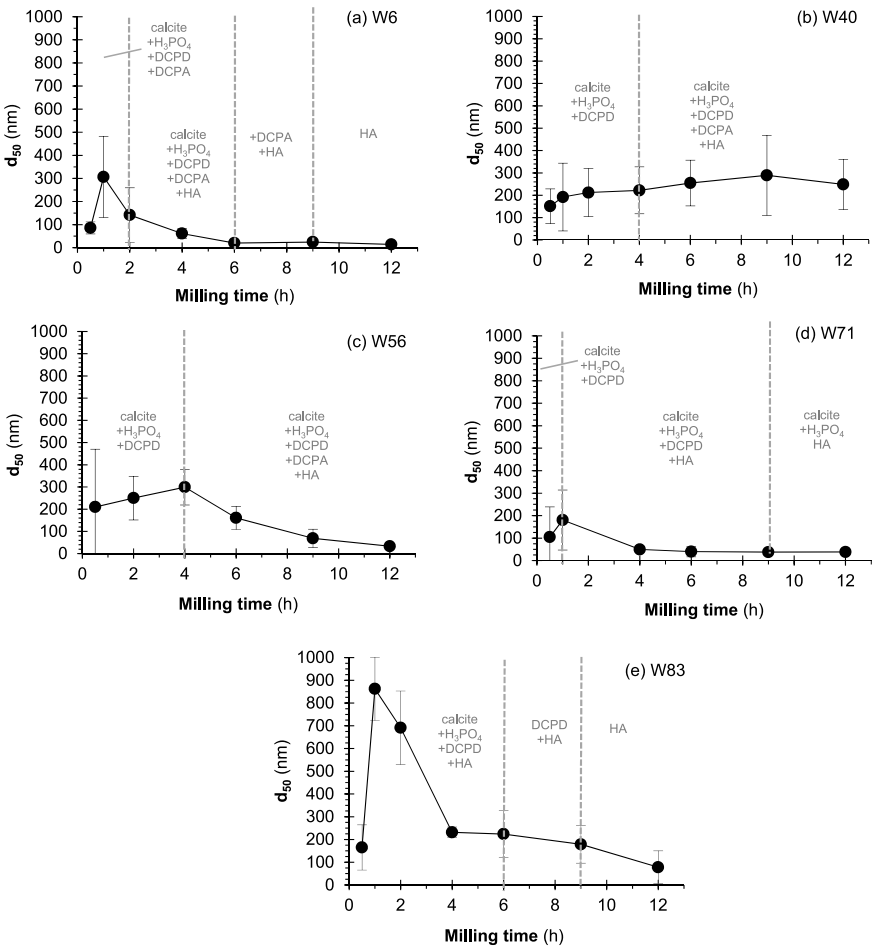

Fig. 9. Evolution of (●) median particle size and standard deviation with increasing milling time: (a) W6, (b) W40, (c) W56, (d) W71, and (e) W83. The solid phases identified in each range are indicated.

domain, from above at least 30 min to above at least 6 h. Correspondingly, the DCPD stability domain extends up to at least 4 h, and the onset of reactions 7 (DCPA precipitation) and 8 (HA precipitation from DCPA) is also delayed to 6 h.

The increase of H_2O concentration in the W71 and W83 systems leads to progressive decrease of the DCPD stability domain, from at least 4 h down to below 1 h and below 0.5 h, respectively. HA formation is prompted at much lower milling times, expectedly taking place by direct transformation of DCPD (reaction 6). Above those milling times and up to at least 9 h (W71) and 6 h (W83) both systems evolve to sequential and simultaneous DCPD and HA formation (reactions 5 and 6, respectively).

The equilibrium thermodynamic reaction path in the $CaCO_3$–H_3PO_4–H_2O (Fig. 11a) appears to be only partially followed in mechanosynthesis (Fig. 11b). In the current work, this corresponds to compositions W71 and W83, where the MCPM→DCPD→HA reaction synthesis (4 → 5→6 chemical reactions, Fig. 11a) takes place. In systems W6 to W56, DCPD transformation into HA is intermediated by DCPA. In these compositions mechanosynthesis appears to follow the MCPM→DCPD→DCPA→HA reaction path (corresponding to 4 → 5→7 → 8 chemical reactions, Fig. 11b).

The room temperature mechanosynthesis reactions promoted by milling are enabled by the energy transferred to the reagents, depending on ball motion, impact frequency and impact power, which are determined by the used operational parameters (mill type; milling rate and time; jar material and volume; ball material, number, and diameter; BPR). This array of parameters (§ 2.2) and the milling time required to produce monophasic HA in the current work – 12 h (Fig. 10), were used to estimate the power and energy required to produce 1 g of HA. The simple kinetic model developed by Burgio [67] indicates that, for the estimated power used in the experiments - 0.16 W/g, an energy value of 6.8 kJ/g is obtained. Additionally, monophasic HA was identified only in compositions W6 and W83, suggesting an ideal range of water concentration values for processing. Whitin the $CaCO_3$–H_3PO_4–H_2O (Ca/P = 1.67) mixtures experimented in the current work, monophasic HA can thus be produced when W is below at least 6 wt% (triggering a mechanism where DCPA intermediates HA formation) or above at least 86 wt % (proceeding via the expected thermodynamic DCPD reaction path).

4.1. *Effect of CO_2 build-up in the milling jar*

The CO_2 build-up in the confined jar volume due to calcite dissolution (reaction 2.1) is expected to affect the system's chemistry and reactions kinetics [68,69], depending on the interplay between attained pH and CO_2 partial pressure (p_{CO2}) increase in the system [68,69]. At NTP, p_{CO2} is close to 3.2×10^{-4} atm [17], and the dissolution rate of calcite is mostly independent of p_{CO2} and mainly takes place below pH 5. The dissolution rate continuously decreases, being very low and almost constant in the 8–10 pH range [70–72]. Progress of calcite dissolution releases CO_2, which dissolves in the liquid phase proportionally to its partial pressure in the jar gaseous phase [73]. When the dissolved CO_2 reaches equilibrium with p_{CO2} ($K_H = 0.038$ mol l^{-1} atm^{-1} at 25 °C [17]), further $CaCO_3$ decarbonation (reaction 2.1) is prevented [74,75]. Dissolved CO_2 speciates into carbonic acid (H_2CO_3), bicarbonate (HCO_3^-) and carbonate (CO_3^{2-}). The established triprotic equilibrium would be expected to decrease the solution pH, leading to further dissolution of

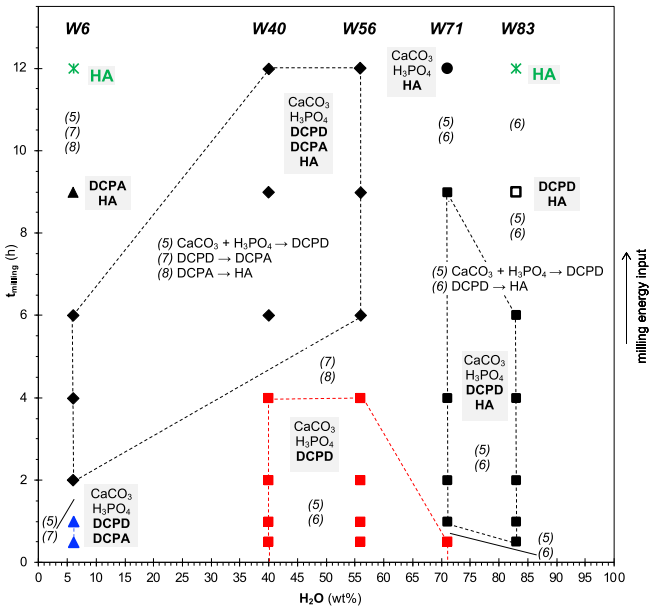

Fig. 10. Preliminary milling map (600 rpm) for the calcite-H_3PO_4–H_2O system (Ca/P = 1.67), showing domains of CaP stability. Dashed lines are tentative boundaries between phases domains. All regions displayed in black (symbols and lines) contain HA; monophasic HA displayed in green. Numeric labels correspond to reactions described in the text (1 and 2.1 omitted). ▲ calcite + H_3PO_4+DCPD + DCPA; ◆ calcite + H_3PO_4+DCPD + DCPA + HA; ▲ DCPA + HA; ✱ HA; ■ calcite + H_3PO_4+DCPD; ■ calcite + H_3PO_4+DCPD + HA; ● calcite + H_3PO_4+HA; □ DCPD + HA. (For interpretation of the references to colour in this figure legend, the reader is referred to the Web version of this article.)

$CaCO_3$ [17,70,72]. Yet, only around 0.3 % CO_2 dissociates into carbonic acid [17], and solution pH is buffered to a value close to 8.4 (the pKa value of HCO_3^-) [17,75]. Since there is no mechanism to remove CO_2, the system pH is reduced changing the stability domains of calcium phosphates and hindering further calcite decomposition [72,74]. Dissolved CO_2 can impact the prevailing Ca/P saturation and the balance between solute concentration and phases solubility [17,70,72], and the extent of carbonate substitution of HA [30]. Further work is ongoing to understand and control the effect of CO_2 build-up upon CaP phases' reaction kinetics, stability and carbonate substitution under high energy milling conditions.

5. Conclusion

This work explores the possibility of synthesising stable calcium phosphates via mechanochemical reaction between calcite, H_3PO_4 and H_2O, using a constant Ca/P ratio of 1.67. Chicken eggshell was used as calcite source. Produced materials include brushite, monetite and hydroxyapatite, confirming that mechanical milling can activate the low-kinetics chemical reactions in the calcite-H_3PO_4–H_2O system, unleashing formation of the thermodynamically stable phases at room temperature. Mechanosynthesis is thus an alternative route to produce tailored calcium phosphate compositions of biomedical significance, including hydroxyapatite. This result importantly dismisses the need of calcite calcination to CaO before milling, which has been universally used as an intermediate step for hydroxyapatite production. All tested compositions apparently evolve to HA formation with increasing milling time. Hydroxyapatite formation appears to follow different reaction sequences, where either brushite or monetite arise as transition product, further converting to HA when milling time increases. Within the tested conditions and analytical methods used, monophasic HA domains are apparently obtained for systems with 6 wt% and 83 wt%-H_2O for a milling energy of 6.8 kJ/g, when a milling power of 0.16 W/g is used (Burgio mechanical milling model). Still, the influence of CO_2 build-up in the system and the control of the drying conditions after milling is mandatory to achieve reproducible final particle composition, morphology, and size distribution. These issues require further study, yet obtained results are very encouraging towards the development of a reproducible and fast method to produce nanometric hydroxyapatite.

Declaration of competing interest

We the undersigned declare that this manuscript is original, has not been published before and is not currently being considered for publication elsewhere.We wish to confirm that there are no known conflicts of interest associated with this publication and there has been no significant financial support for this work that could have influenced its

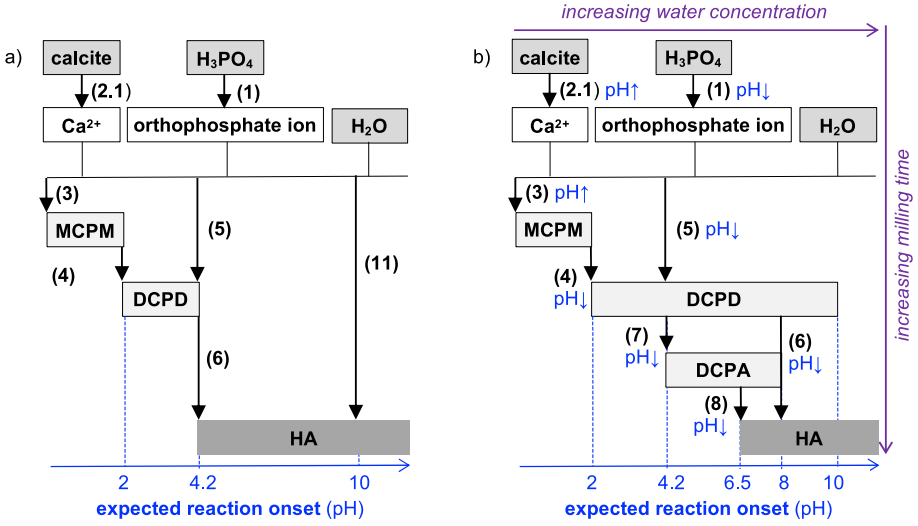

Fig. 11. Schematic representation of $CaCO_3$–H_3PO_4–H_2O reaction paths (Ca/P = 1.67). (a) Reaction sequence admitting that thermodynamic equilibrium is reached in each reaction step, as reported in the literature. (b) Suggested mechanochemical reaction sequence leading to formation of the calcium phosphates identified in this work, including the non-equilibrium intermediate phase DCPA. (Numeric labels correspond to reactions described in the text; purple arrows: provided experimental conditions; blue arrows: pH values, segments not at scale). (For interpretation of the references to colour in this figure legend, the reader is referred to the Web version of this article.)

outcome.We confirm that the manuscript has been read and approved by all named authors and that there are no other persons who satisfied the criteria for authorship but are not listed. We further confirm that the order of authors listed in the manuscript has been approved by all of us. We confirm that we have given due consideration to the protection of intellectual property associated with this work and that there are no impediments to publication, including the timing of publication, with respect to intellectual property. In so doing we confirm that we have followed the regulations of our institutions concerning intellectual property.We understand that the Corresponding Author is the sole contact for the Editorial process (including Editorial Manager and direct communications with the office). He/she is responsible for communicating with the other authors about progress, submissions of revisions and final approval of proofs. We confirm that we have provided a current, correct email address which is accessible by the Corresponding Author.

Acknowledgements

This work was supported by FCT under contract UIDB/04540/2020 (through CeFEMA), under project PTDC/ECI-COM-28308/2017. T.S. is grateful to FCT for the Doctoral Grant 2022.10551.BD.

Appendix A. Supplementary data

Supplementary data to this article can be found online at https://doi.org/10.1016/j.ceramint.2023.10.102.

References

[1] C. Elliot, Chapter 18: general chemistry of the calcium orthophosphates, in: Stud. Inorg. Chem., Elsevier, 1994, pp. 1–62, https://doi.org/10.1016/B978-0-444-81582-8.50006-7.
[2] S.V. Dorozhkin, Calcium orthophosphates: occurrence, properties, biomineralization, pathological calcification and biomimetic applications, Biomaterials 1 (2011) 121–164.
[3] J.D. Pasteris, A mineralogical view of apatitic biomaterials, Am. Mineral. 101 (2016) 2594. LP – 2610, http://ammin.geoscienceworld.org/content/101/12/2594.abstract.
[4] G. Turnbull, J. Clarke, F. Picard, P. Riches, L. Jia, F. Han, et al., 3D bioactive composite scaffolds for bone tissue engineering, Bioact. Mater. 3 (2018) 278–314, https://doi.org/10.1016/J.BIOACTMAT.2017.10.001.
[5] S. Stratton, N.B. Shelke, K. Hoshino, S. Rudraiah, S.G. Kumbar, Bioactive polymeric scaffolds for tissue engineering, Bioact. Mater. 1 (2016) 93–108, https://doi.org/10.1016/J.BIOACTMAT.2016.11.001.
[6] R.Z. LeGeros, Properties of osteoconductive biomaterials: calcium phosphates, Clin. Orthop. Relat. Res. 395 (2002) 81–98.
[7] M. Sadat-Shojai, M.-T. Khorasani, E. Dinpanah-Khoshdargi, A. Jamshidi, Synthesis methods for nanosized hydroxyapatite with diverse structures, Acta Biomater. 9 (2013) 7591–7621, https://doi.org/10.1016/j.actbio.2013.04.012.
[8] S.V. Dorozhkin, Calcium orthophosphate (CaPO4) scaffolds for bone tissue engineering applications, J. Biotechnol. Biomed. Sci. 1 (2018) 25–93.
[9] G.L. Koons, M. Diba, A.G. Mikos, Materials design for bone-tissue engineering, Nat. Rev. Mater. 5 (2020) 584–603, https://doi.org/10.1038/s41578-020-0204-2.
[10] S.V. Dorozhkin, Calcium orthophosphates in nature, biology and medicine, Materials 2 (2009) 399–498.
[11] J.S. Clark, R.C. Turner, Reactions between solid calcium carbonate and orthophosphate solutions, Can. J. Chem. 33 (1955) 665–671.
[12] C.V. Cole, S.R. Olsen, C.O. Scott, The nature of phosphate sporption by calcium carbonate, Soil Sci. Soc. Am. Proc. 17 (1953) 352.
[13] D.P. Minh, N. Lyczko, H. Sebei, A. Nzihou, P. Sharrock, Synthesis of calcium hydroxyapatite from calcium carbonate and different orthophosphate sources: a comparative study, Mater. Sci. Eng. B 177 (2012) 1080–1089, https://doi.org/10.1016/J.MSEB.2012.05.007.
[14] R.I. Martin, P.W. Brown, Phase equilibria among acid calcium phosphates, J. Am. Ceram. Soc. 80 (1997) 1263–1266, https://doi.org/10.1111/j.1151-2916.1997.tb02973.x.
[15] L. Wang, G.H. Nancollas, Calcium orthophosphates: crystallization and dissolution, Chem. Rev. 108 (2008) 4628–4669, https://doi.org/10.1021/cr0782574.
[16] D.-P. Minh, N.D. Tran, A. Nzihou, P. Sharrock, One-step synthesis of calcium hydroxyapatite from calcium carbonate and orthophosphoric acid under moderate conditions, Ind. Eng. Chem. Res. 52 (2013) 1439–1447, https://doi.org/10.1021/ie302422d.
[17] C.B. Andersen, Understanding carbonate equilibria by measuring alkalinity in experimental and natural systems, J. Geosci. Educ. 50 (2002) 389–403, https://doi.org/10.5408/1089-9995-50.4.389.
[18] Y. Bai, Q. Bai, Subsea corrosion and scale, in: Subsea Eng. Handb., Elsevier, 2019, pp. 455–487, https://doi.org/10.1016/b978-0-12-812622-6.00017-8.
[19] S. Aghajanian, H. Nieminen, T. Koiranen, Precipitation of calcium carbonate in highly alkaline solution through carbonated water, in: Proc. Second Int. Process Intensif. Conf., 2019. Leuven, www.tomocon.eu/wp-content/upload.
[20] E. Fernandez, F.J. Gil, M.P. Ginebra, F.C.M. Driessens, J.A. Planell, S.M. Best, Calcium phosphate bone cements for clinical applications. Part II: precipitate formation during setting reactions, J. Mater. Sci. Mater. Med. 10 (1999) 177–183, https://doi.org/10.1023/A:1008989525461.
[21] P.W. Brown, N. Hocker, S. Hoyle, Variations in solution chemistry during the low-temperature formation of hydroxyapatite, J. Am. Ceram. Soc. 74 (1991) 1848–1854, https://doi.org/10.1111/j.1151-2916.1991.tb07798.x.
[22] L. Chou, R.M. Garrels, R. Wollast, Comparative study of the kinetics and mechanisms of dissolution of carbonate minerals, Chem. Geol. 78 (1989) 269–282, https://doi.org/10.1016/0009-2541(89)90063-6.
[23] M.D. Francis, N.C. Webb, Hydroxyapatite formation from a hydrated calcium monohydrogen phosphate precursor, Calcif. Tissue Res. 6 (1971) 335–342, https://doi.org/10.1007/BF02196214.
[24] H. Ehrlich, P.G. Koutsoukos, K.D. Demadis, O.S. Pokrovsky, Principles of demineralization: modern strategies for the isolation of organic frameworks. Part II, Decalcification, Micron 40 (2009) 169–193, https://doi.org/10.1016/j.micron.2008.06.004.
[25] C. Oliveira, A. Ferreira, F. Rocha, Dicalcium phosphate dihydrate precipitation: characterization and crystal growth, Chem. Eng. Res. Des. 85 (2007) 1655–1661, https://doi.org/10.1016/S0263-8762(07)73209-4.
[26] D. Wu, M. Guo, G. Ma, F. Niu, Dilution characteristics of ultrasonic assisted laser clad yttria-stabilized zirconia coating, Mater. Lett. 141 (2015) 207–209, https://doi.org/10.1016/j.matlet.2014.11.058.
[27] M.S. Tung, L.C. Chow, W.E. Brown, Hydrolysis of dicalcium phosphate dihydrate in the presence or absence of calcium fluoride, J. Dent. Res. 64 (1985) 2–5, https://doi.org/10.1177/00220345850640010301.
[28] M.T. Fulmer, P.W. Brown, Hydrolysis of dicalcium phosphate dihydrate to hydroxyapatite, J. Mater. Sci. Mater. Med. 9 (1998) 197–202.
[29] F. Cestari, G. Chemello, A. Galotta, V.M. Sglavo, Low-temperature synthesis of nanometric apatite from biogenic sources, Ceram. Int. 46 (2020) 23526–23533, https://doi.org/10.1016/j.ceramint.2020.06.123.
[30] C. Rey, C. Combes, C. Drouet, D. Grossin, Bioactive ceramics: physical chemistry, in: P. Ducheyne, K. Healy, D. Hutmacher, D.E. Grainger, J. Kirkpatrick (Eds.), Compr. Biomater., Elsevier, 2011, pp. 187–221.
[31] D.S. Gomes, A.M.C. Santos, G.A. Neves, R.R. Menezes, D.S. Gomes, A.M.C. Santos, et al., A brief review on hydroxyapatite production and use in biomedicine, Cerâmica 65 (2019) 282–302, https://doi.org/10.1590/0366-69132019653742706.
[32] B. Ahmed, C.J. Brown, T. McGlone, D.L. Bowering, J. Sefcik, A.J. Florence, Engineering of acetaminophen particle attributes using a wet milling crystallisation platform, Int. J. Pharm. 554 (2019) 201–211, https://doi.org/10.1016/j.ijpharm.2018.10.073.
[33] P. Balaz, M. Achimovicova, M. Balaz, P. Billik, Z. Cherkezova-Zheleva, J.M. Criado, et al., Hallmarks of mechanochemistry: from nanoparticles to technology, Chem. Soc. Rev. 42 (2013) 7571–7637, https://doi.org/10.1039/C3CS35468G.
[34] Y. Wang, L. Liu, S. Guo, Characterization of biodegradable and cytocompatible nano-hydroxyapatite/polycaprolactone porous scaffolds in degradation in vitro, Polym. Degrad. Stabil. 95 (2010) 207–213.
[35] L. Wang, G.H. Nancollas, Pathways to biomineralization and biodemineralization of calcium phosphates: the thermodynamic and kinetic controls, Dalton Trans. (2009) 2665–2672.
[36] S.V. Dorozhkin, Nanosized and nanocrystalline calcium orthophosphates, Acta Biomater. 6 (2010) 715–734, https://doi.org/10.1016/J.ACTBIO.2009.10.031.
[37] Y. Cai, Y. Liu, W. Yan, Q. Hu, J. Tao, M. Zhang, Role of hydroxyapatite nanoparticle size in bone cell proliferation, J. Mater. Chem. 17 (2007) 3780–3787. J Mater Chem. 17 (2007) 3780–3787.
[38] S.-C. Wu, H.-C. Hsu, S.-K. Hsu, Y.-C. Chang, W.-F. Ho, Effects of heat treatment on the synthesis of hydroxyapatite from eggshell powders, Ceram. Int. 41 (2015) 10718–10724, https://doi.org/10.1016/j.ceramint.2015.05.006.
[39] W.-F. Ho, H.-C. Hsu, S.-K. Hsu, C.-W. Hung, S.-C. Wu, Calcium phosphate bioceramics synthesized from eggshell powders through a solid state reaction, Ceram. Int. 39 (2013) 6467–6473, https://doi.org/10.1016/j.ceramint.2013.01.076.
[40] M. Šupová, Substituted hydroxyapatites for biomedical applications: a review, Ceram. Int. 41 (2015) 9203–9231, https://doi.org/10.1016/J.CERAMINT.2015.03.316.
[41] S.-W. Lee, C. Balázsi, K. Balázsi, D. Seo, H.S. Kim, C.-H. Kim, et al., Comparative Study of hydroxyapatite prepared from seashells and eggshells as a bone graft material, Tissue Eng. Regen. Med. 11 (2014) 113–120, https://doi.org/10.1007/s13770-014-0056-1.
[42] S.J. Lee, S.H. Oh, Fabrication of calcium phosphate bioceramics by using eggshell and phosphoric acid, Mater. Lett. 57 (2003) 4570–4574, https://doi.org/10.1016/S0167-577X(03)00363-X.
[43] A.A. Francis, M.K.A. Rahman, The environmental sustainability of calcined calcium phosphates production from the milling of eggshell wastes and phosphoric acid, J. Clean. Prod. 137 (2016) 1432–1438, https://doi.org/10.1016/j.jclepro.2016.08.029.
[44] A.C. Ferro, M. Guedes, Mechanochemical synthesis of hydroxyapatite using cuttlefish bone and chicken eggshell as calcium precursors, Mater. Sci. Eng. C 97 (2019) 124–140, https://doi.org/10.1016/J.MSEC.2018.11.083.

[45] C.A. Schneider, W.S. Rasband, K.W. Eliceiri, NIH Image to ImageJ: 25 years of image analysis, Nat. Methods 9 (2012) 671–675, https://doi.org/10.1038/nmeth.2089.
[46] M. Wojdyr, Fityk: a general-purpose peak fitting program, J. Appl. Crystallogr. 43 (2010) 1126–1128.
[47] H.G.M. Edwards, S.J. Villar, J. Jehlicka, T. Munshi, FT–Raman spectroscopic study of calcium-rich and magnesium-rich carbonate minerals, Spectrochim. Acta Part A Mol. Biomol. Spectrosc. 61 (2005) 2273–2280, https://doi.org/10.1016/J.SAA.2005.02.026.
[48] T. Schmid, P. Dariz, Shedding light onto the spectra of lime: Raman and luminescence bands of CaO, Ca(OH)2 and CaCO3, J. Raman Spectrosc. 46 (2015) 141–146, https://doi.org/10.1002/jrs.4622.
[49] D.B. Thomas, M.E. Hauber, D. Hanley, G.I.N. Waterhouse, S. Fraser, K.C. Gordon, Analysing avian eggshell pigments with Raman spectroscopy, J. Exp. Biol. 218 (2015) 2670–2674. http://jeb.biologists.org/content/218/17/2670.abstract.
[50] W.W. Rudolph, Raman- and infrared-spectroscopic investigations of dilute aqueous phosphoric acid solutions, Dalton Trans. 39 (2010) 9642–9653.
[51] J. Lewis, D. Schwarzenbach, H.D. Flack, Electric field gradients and charge density in corundum, α-Al2O3, Acta Crystallogr., Sect. A 38 (1982) 733–739, https://doi.org/10.1107/S0567739482001478.
[52] J. Xu, I.S. Butler, D.F.R. Gilson, FT-Raman and high-pressure infrared spectroscopic studies of dicalcium phosphate dihydrate (CaHPO4·2H2O) and anhydrous dicalcium phosphate (CaHPO4), Spectrochim, Acta Part A Mol. Biomol. Spectrosc. 55 (1999) 2801–2809, https://doi.org/10.1016/S1386-1425(99)00090-6.
[53] S. Koutsopoulos, Synthesis and characterization of hydroxyapatite crystals: a review study on the analytical methods, J. Biomed. Mater. Res. 62 (2002) 600–612.
[54] C. Combes, C. Rey, Amorphous calcium phosphates: synthesis, properties and uses in biomaterials, Acta Biomater. 6 (2010) 3362–3378, https://doi.org/10.1016/j.actbio.2010.02.017.
[55] E.M. Moroz, X-Ray diffraction structure diagnostics of nanomaterials, Russ. Chem. Rev. 80 (2011) 293–312, https://doi.org/10.1070/RC2011v080n04ABEH004163.
[56] M.A. Lopez-Heredia, M. Bohner, W. Zhou, A.J.A. Winnubst, J.G.C. Wolke, J. A. Jansen, The effect of ball milling grinding pathways on the bulk and reactivity properties of calcium phosphate cements, J. Biomed. Mater. Res. Part B Appl. Biomater. 98B (2011) 68–79, https://doi.org/10.1002/jbm.b.31833.
[57] J. McGinty, N. Yazdanpanah, C. Price, J.H. ter Horst, J. Sefcik, Chapter 1: nucleation and crystal growth in continuous crystallization, in: Handb. Contin. Cryst., Royal Society of Chemistry, 2020, pp. 1–50.
[58] T. Kozawa, K. Fukuyama, A. Kondo, M. Naito, Wet mechanical route to synthesize morphology-controlled NH4MnPO4·H2O and its conversion reaction into LiMnPO4, ACS Omega 4 (2019) 5690–5695, https://doi.org/10.1021/acsomega.9b00026.
[59] T. Kozawa, K. Fukuyama, A. Kondo, M. Naito, Wet milling synthesis of NH4CoPO4·H2O platelets: formation reaction, growth mechanism, and conversion into high-voltage LiCoPO4 cathode for Li-ion batteries, Mater. Res. Bull. 135 (2021), 111149, https://doi.org/10.1016/J.MATERRESBULL.2020.111149.
[60] T. Toshima, R. Hamai, M. Tafu, Y. Takemura, S. Fujita, T. Chohji, et al., Morphology control of brushite prepared by aqueous solution synthesis, J. Asian Ceram. Soc. 2 (2014) 52–56, https://doi.org/10.1016/J.JASCER.2014.01.004.
[61] A.C. Tas, Monetite (CaHPO4) synthesis in ethanol at room temperature, J. Am. Ceram. Soc. 92 (2009) 2907–2912, https://doi.org/10.1111/j.1551-2916.2009.03351.x.
[62] K.V. Nishad, S. Sureshbabu, M. Komath, G. Unnikrishnan, Synthesis and characterization of low dimensional bioactive monetite by solvent exchange method, Mater. Lett. 209 (2017) 19–22, https://doi.org/10.1016/J.MATLET.2017.07.104.
[63] E. Mhla, P.G. Koutsoukos, Heterogeneous crystallization of calcium hydrogen phosphate anhydrous (monetite), Colloids Surfaces A Physicochem. Eng. Asp. 513 (2017) 125–135, https://doi.org/10.1016/J.COLSURFA.2016.11.041.
[64] O.S. Pokrovsky, S.V. Golubev, J. Schott, A. Castillo, Calcite, dolomite and magnesite dissolution kinetics in aqueous solutions at acid to circumneutral pH, 25 to 150 °C and 1 to 55 atm pCO2: new constraints on CO2 sequestration in sedimentary basins, Chem. Geol. 265 (2009) 20–32, https://doi.org/10.1016/J.CHEMGEO.2009.01.013.
[65] O.S. Pokrovsky, S.V. Golubev, J. Schott, Dissolution kinetics of calcite, dolomite and magnesite at 25 °C and 0 to 50 atm pCO2, Chem. Geol. 217 (2005) 239–255, https://doi.org/10.1016/J.CHEMGEO.2004.12.012.
[66] W. Kim, F. Saito, Sonochemical synthesis of hydroxyapatite from H3PO4 solution with Ca(OH)2, Ultrason. Sonochem. 8 (2001) 85–88, https://doi.org/10.1016/S1350-4177(00)00034-1.
[67] N. Burgio, A. Iasonna, M. Magini, S. Martelli, F. Padella, Mechanical alloying of the Fe−Zr system. Correlation between input energy and end products, Nuovo Cim. D. 13 (1991) 459–476, https://doi.org/10.1007/BF02452130.
[68] C. Peng, J.P. Crawshaw, G.C. Maitland, J.P.M. Trusler, Kinetics of calcite dissolution in CO2-saturated water at temperatures between (323 and 373) K and pressures up to 13.8 MPa, Chem. Geol. 403 (2015) 74–85, https://doi.org/10.1016/J.CHEMGEO.2015.03.012.
[69] C. Peng, J.P. Crawshaw, G.C. Maitland, J.P. Martin Trusler, D. Vega-Maza, The pH of CO2-saturated water at temperatures between 308 K and 423 K at pressures up to 15 MPa, J. Supercrit. Fluids 82 (2013) 129–137, https://doi.org/10.1016/j.supflu.2013.07.001.
[70] I.V. Dolgaleva, I.G. Gorichev, A.D. Izotov, V.M. Stepanov, Modeling of the effect of pH on the calcite dissolution kinetics, Theor. Found. Chem. Eng. 39 (2005) 614–621, https://doi.org/10.1007/s11236-005-0125-1.
[71] T. Tenno, K. Uiga, A. Mashirin, I. Zekker, E. Rikmann, Modeling closed equilibrium systems of H2O–dissolved CO2–solid CaCO3, J. Phys. Chem. A 121 (2017) 3094–3100, https://doi.org/10.1021/acs.jpca.7b00237.
[72] G. Vereecke, J. Lemaître, Calculation of the solubility diagrams in the system Ca(OH)2-H3PO4-KOH-HNO3-CO2-H2O, J. Cryst. Growth 104 (1990) 820–832.
[73] P. von Paris, J.L. Grenfell, P. Hedelt, H. Rauer, F. Selsis, B. Stracke, Atmospheric constraints for the CO2 partial pressure on terrestrial planets near the outer edge of the habitable zone, A&A 549 (2013), https://doi.org/10.1051/0004-6361/201219684.
[74] Z. Bakher, M. Kaddami, Thermodynamic equilibrium in the system H2O+P2O5+CaCO3 at 25 and 70 °C: application for synthesis of calcium phosphate products based on calcium carbonate decomposition, Fluid Phase Equil. 456 (2018) 46–56, https://doi.org/10.1016/J.FLUID.2017.10.005.
[75] P.W. Hart, G.W. Colson, J. Burris, Application of carbon dioxide to reduce water-side lime scale in heat exchangers, J. Sci. Technol. For. Prod. Process. 1 (2011) 67–70.